Chemistry Europe
European Chemical Societies Publishing

WILEY VCH

Excellence in Chemistry Research

Announcing our new flagship journal

- Gold Open Access
- Publishing charges waived
- Preprints welcome
- Edited by active scientists

Meet the Editors of *ChemistryEurope*

Luisa De Cola
Università degli Studi di Milano Statale, Italy

Ive Hermans
University of Wisconsin-Madison, USA

Ken Tanaka
Tokyo Institute of Technology, Japan

ChemistrySelect

Research Article
doi.org/10.1002/slct.202204305

Chemistry Europe
European Chemical Societies Publishing

www.chemistryselect.org

Activation of NO_2 by Modifying the Porphyrin Unit with Oxygen in a MnN_4 Graphene Layer

Ali Emre Genç,*[a] Hilal Küçük,[a] and Aykan Akça[b]

In this article, the activation of N–O bonds in NO_2 molecules has been investigated by Density Functional Theory (DFT) calculations. Considering the graphene-based MnN_4 layer, nitrogen atoms in the porphyrin unit were sequentially replaced with oxygen atoms to create different MnN_mO_n/G ($m+n=4$ and $1<m\leq 4$) layers. As more oxygen atoms are incorporated in porphyrin units for bare layers, the covalent character of the Mn–O bonds is switched to the transit nature with respect to Mn–N bonds. Moreover, the trend in bond strength decreasing in all oxygen-containing bonds is in line with the formation energy trends of bare layers. The same situation is also valid for the bonds between Mn–N/O. For NO_2 adsorption configurations on all MnN_mO_n/G layers, N–O bonds in NO_2 are weakened by populating/depopulating antibonding/bonding orbitals, respectively. Even if the MnN_2O_2(hex)/G layer has a moderate NO_2 adsorption energy among the other layers, this layer provided the most significant activation over N–O bonds based on crystal orbital Hamilton population (COHP), crystal orbital bond index (COBI), and Atoms in Molecules (AIM) Bader Topological Analysis. Our results show that integrated COHP and integrated COBI values show a remarkable correlation with AIM-Bader parameters for the specific bonds which have descriptive capability over NO_2 molecule activation.

Introduction

As known, NO_x gases are very harmful to human nature and the ecosystem on earth. Nitrogen oxides irritate skin and cause various diseases such as respiratory illnesses, Parkinson's disease, pneumonia, etc.[1,2] Approximately, 90% of the NO_x species are released by the combustion of the fossil fuels.[3] In urban regions, NO_2 (nitrogen dioxide) is one of the major components of the toxic gases which can easily react with the other chemical species and the ozone molecule.[4,5] To eliminate NO_2 from the atmosphere, there are some strategies such as capturing and reducing it to other less harmful chemicals by reacting with the other chemicals.[6–8] Before handling any strategy, NO_2 molecule should be captured with an acceptable adsorption energy on the active sites of the catalytic material and activated for conversion to the other chemicals. For this kind of capture and catalytic applications, Graphene received spectacular interest since it was fabricated.[9,10] Because pure Graphene is inert towards chemical reactions and has some drawbacks to its usage as a capture material,[11–13] various strategies can be applied to enhance its activity such as doping foreign atoms, creating vacancies, embedding foreign atoms into the different kind of vacancies and functionalizing by substitution of different p and d-block elements.[14–20]

So far, a large number of publications aimed to investigate NO_2 interaction mechanism with the functionalized two-dimensional (2D) catalytic surfaces because this is the first step of aim no matter what the application is.[21–30] Liang and colleague have investigated the NO_2 adsorption characteristics on Mn-embedded carbon materials including MnN_4 graphene layer. They found that MnN_4 is suitable substrate to capture NO_2 molecule with an acceptable adsorption energy.[31] Even if a large number of publications are aiming to investigate NO_2 adsorption, relatively few of them considered the chemical bonding analysis. According to the Kaewmaraya, NO_2 has the largest adsorption energy among the hazardous gas molecules. Moreover, S-doped GreenP layer is populating antibonding orbitals from the COHP plots between Sulphur on the layer and nitrogen in the molecule to some extent.[32] Nanda and his co-workers investigated the NO_2 dissociation in the presence and absence of water on rutile $TiO_2(110)$ surface. They concluded that NO_2 adsorption is in physisorptive without water. Another key finding is that the antibonding orbital population between Ti and On atoms has been found insignificant from the COHP figures.[33]

In recent years, graphene-based porphyrin-like transition metal-nitrogen-carbon layers (herein after TMN_4) successfully fabricated and tested for their potential activities for many reactions.[16,34–36] Among these TMN_4 layers, MnN_4 has been showed to have promising properties for oxygen reduction reaction (ORR), toxic gas sensing, carbon monoxide oxidation, etc..[37–41] Exchanging nitrogen atoms with p-type atoms in a porphyrin unit has been typically tested to elevate the catalytic activity of MnN_4 graphene layer upon various applications. The synthesis of atomically dispersed oxygen and nitrogen in porphyrin has been recently realized by experiments to have MnN_mO_n/G ($m+n=4$ *and* $1<m\leq 4$) motifs. According to the findings of Yang et al. showed that oxygen incorporation

[a] *Dr. A. Emre Genç, Dr. H. Küçük*
Gazi University, Faculty of Science, Department of Physics, 06500, Ankara, Turkey
Tel: +90 3122021457
E-mail: aegenc@gazi.edu.tr
[b] *Dr. A. Akça*
Aksaray University, Faculty of Science and Art, Department of Physics, 68100, Aksaray, Turkey

Supporting information for this article is available on the WWW under https://doi.org/10.1002/slct.202204305

into the porphyrin unit greatly enhances the ORR performance.[42] In another publication by Xin and Liu, the NRR (nitrogen reduction reaction) performance of the $MnNO_3$/G layer is boosted through oxygen incorporation into porphyrin unit. They also found that the initial N_2 adsorption strength is elevated and the stabilization of the NNH which is first protonated NRR reaction intermediate is enhanced.[43] A short literature survey shows that MnN_mO_n/G layer have potential activity for different kind of catalytic reactions.

In this article, NO_2 adsorption is investigated on six MnN_mO_n/G layers and activation of intramolecular N–O bonds are elaborately clarified using AIM-Bader Topological Analysis (AIM-BTA) and COHP/COBI analysis. Details will be given and discussed in the computational methods section. Bader topological analysis is a traditional and powerful tool to elucidate bonding types in any atomic or molecular circumstance. Although COHP analysis is used widely for periodic systems by chemical society, AIM-BTA is generally used in molecular structures. This will be one of the first articles using AIM-BTA and COHP analyses for 2-D periodic systems, simultaneously. Herein, we first describe how the chemical bonding environment is changed by oxygen incorporation into the porphyrin unit on MnN_4 layer. It is found that as more oxygen is substituted with nitrogen atoms, bond strengths between Mn and surrounding atoms are weakened and become more ionic. For the NO_2 adsorption, as more oxygen is incorporated into porphyrin units, the degree of the population of bonding and antibonding orbitals are changed. More interestingly, the formation energies of the layers and NO_2 adsorption energies correlate with AIM-Bader parameters along with the ICOHP and ICOBI values. AIM-Bader and ICOHP/ICOBI parameters show a good correlation for specific bonds.

Computational Methods

Periodic density functional theory calculations have been carried out via Quantum Espresso simulation package.[44–46] PAW-type pseudopotentials have been used to depict ion-electron interactions, while the exchange-correlation effect has been treated by PBE functional.[47–49] The energy cut-off value has been selected as 80 Ry (800 Ry for charge density) for extending plane waves over the Brillouin zone. The gaussian smearing and a 0.07 Ry degauss value have been used for the Brillouin zone integration. The Brillouin zone integration belonging to real lattices, which has a = b = 12.33 Å lattice parameters, were sampled by 4x4x1 and 12x12x1 Mokhorst-Pack k-point sets for the geometric optimizations and for the further electronic structure analyses (i.e. partial density of states (PDOS), electron density differences (EDD) and all-electron Bader charge and COHP analysis).[50–53] A vacuum depth was taken as 20 Å to eliminate undesirable interaction between repetitive images along the z-direction. Grimme-D3 dispersion correction has been taken into consideration to obtain better geometries and energies for surface-molecule interactions. The most stable geometry of the molecules has been calculated in a cube with a P1 symmetry and 20 Å side length in each direction. Brilluoin zone sampling for gas phase geometric optimizations and further electronic analyses carried out at gamma point. The structural relaxations for surface-molecule interactions were ceased after reaching the convergence thresholds for ionic minimizations, selfconsistency, and atomic forces, of 10^{-6} Ry, 10^{-6} Ry and 10^{-6} Ry/Bohr, respectively.

To create a model layer, a 5x5 graphene layer was produced using optimized graphite crystal. Then, in the middle of the layer carbon divacancy has been created. The neighbor 4 carbon atoms to the divacancy have been replaced with the nitrogen atoms. Finally, Mn atom is positioned in the middle of these 4 nitrogen atoms. In the subsequent structures, the N atoms were sequentially exchanged with oxygen atoms MnN_mO_n/G ($m+n=4$ *and* $1<m\leq 4$). To identify the stability of the structures, the formation energies of all the considered structures were calculated according to Equation (1):

$$E_f = E_{system} + 6\mu_C - m\mu_N - n\mu_O - E_{Mn-atom} - E_{Gra};\ (m+n=4) \quad (1)$$

In Equation (1), the 1st term represents the total energy of the system, 2nd, 3rd, and 4th terms are the total chemical potentials of the missing 6 carbon atoms (2 coming from the divacancy, and 4 substituted initially by N atoms), and of the *mN* atoms and *nO* atoms, respectively; the 5th term is the total energy of the single Mn atom, while the 6th is the total energy of the pure graphene layer composed of 50 carbon atoms. The chemical potentials of the O and N atoms were calculated by taking half of the gas phase total energies of O_2 and N_2 molecules, respectively, while that of the C atom was obtained from a periodic graphene calculation.

Adsorption energies were calculated according to Equation (2),

$$E_{ads} = E_{adsorbates/MnN_mO_n} - (E_{MnN_mO_n} + E_{adsorbates}) \quad (2)$$

In Equation (2), 1st, 2nd, and the 3rd terms are the total energies of the interacted system, of the bare MnN_mO_n $(m+n=4,\ m\neq 0)$ graphene layer and that of the reaction intermediates.

Electron Density Differences (EDD) were calculated by subtracting the individual charge densities of the adsorbates and of the functionalized graphene layer from the interacted system:

$$\Delta\rho_{ads} = \rho_{system} - \rho_{adsorbates} - \rho_{MnN_mO_n} \quad (3)$$

Chemical bonding information related to some descriptive bonds to clarify bonding nature in layers and adsorbed configurations have been gathered in two different ways. First, AIM-Bader Topological analysis has been used to identify bond types under consideration.[54] In this analysis, the three-dimensional electron density is divided into subsystems containing one nucleus. Electron density is the maximum on the atoms and its tail decays exponentially towards the interatomic region and zero-flux surfaces are formed. The connection point of this decaying electron density is called "Bond Critical Points (BCP)". Using Bader partitioning scheme, bonds between atoms have BCP and characterize bonds where the electron density variation is zero ($\vec{\nabla}\vec{\rho}=0$).[54,55] In principle, two bonded atoms should have a BCP and some properties of this BCP give an implication regarding bonding type. The most important feature is the Laplacian which is the second derivative of the electron density is $\nabla^2\cdot\rho$. Its sign gives information about BCP topology. A negative sign of the Laplacian points towards a covalent bond, while a positive Laplacian is indicative of an ionic bond. So far, the ratio of the potential and kinetic energy densities ($|V|/G$); total energy density per electron (H/ρ, where $H=G(\vec{r})+\mathcal{V}(\vec{r})$) have been seen as very powerful

descriptors to clarify bond type.[55–58] The balance between kinetic and potential energy densities determines the bond type. Because potential energy density is the average virial field felt by an electron at BCP, it is always negative. If potential and kinetic energy densities dominate at related BCP, covalent and ionic bonds overwhelm, respectively. Correspondingly, more negative and positive total energy values indicate more ionic and more covalent bonds, respectively. For the ratio of the potential and kinetic energy densities ($|V|/G$), when potential energy dominates this quantity gets a larger value than 1 and indicates more ionic character. When this quantity gets a smaller value than 1, the bond becomes more covalent. Considering AIM-Bader parameters explained above, Table 1 can be used to summarize bonding types according to the article of Gatti.[59] In Table 1, transit bonds that have different rates of the contribution of kinetic and potential energy densities can be defined.

In this article, BCPs have been determined using Topchem2 software.[60,61] Topchem2 software uses Gaussian type *.cube files to generate BCPs and can be easily operated on Quantum Espresso using all-electron density generated by Bader code.

Another tool for gathering information about chemical bonds and their types is Crystal orbital Hamilton population (COHP) which utilizes electronic wave functions to generate bonding information. In this method, the plane wave function is converted to the wave function which is a collection of linear combinations of atomic orbitals.[62–67] In other words, band structure energies are partitioned into atoms (on-site) and bonds (off-site) contributions. Crystal Orbital Bond Index (COBI) is a new quantity that defines the nature of the bonds based on the bond index of Wiberg and Mayer adapted for the crystals.[68–70] Integrated crystal orbital Hamilton populations (ICOHP) and integrated crystal orbital bond index (ICOBI) values have been taken into consideration to analyze chemical bonding information. For ICOHP, more negative values imply increasing covalent character and stronger bond, while the less negative values show the ionic character of the bond. For ICOBI, the perfect covalent bond is shown by an index, a very close value of one, while the perfect ionic bond has a very close value of zero. For ICOHP and ICOBI, it is also possible to get orbital projected contributions to overall quantities. Crystal orbital Hamilton populations (COHP) plots were used to analyze electron densities over the bonding and antibonding orbitals in parallel with a partial density of states (PDOS). In this article, COHP calculations have been carried out using Lobster code with its 4.0.0 version.[71] The total ICOHP value of each bond has been generated by summing spin-up and spin-down components. Figures have been prepared by Material Studio 6.0 interface.[72]

Table 1. Parameter intervals for different bonding types in AIM-Bader.[59] All parameters here are in atomic units (a.u.).

Bond Type	$\nabla^2\rho$	$\lvert V\rvert/G$	H/ρ
Covalent	<0	>2	<0
Transit	>0	$1<\ldots<2$	≈ 0
Ionic, vdW	>0	<1	>0

Table 2. AIM-Bader, ICOHP, and ICOBI parameters for each N–O bond in NO_2 molecule. AIM-Bader parameters are all in atomic units (a.u.).

Bonds	$\nabla^2\rho$	$\lvert V\rvert/G$	H/ρ	ICOHP(eV)	ICOBI
Bond 1	−1.43	2.60	−2.14	−8.41	0.81
Bond 2	−1.41	2.59	−2.15	−8.41	0.81

Results and Discussions

Electronic and chemical bonding features of NO_2

Primarily, some electronic and chemical bonding data have been gathered for NO_2 molecule in the gas phase. After geometric optimizations, each N–O bond length and bond angle were measured as 1.21 Å and 133.3°, respectively as seen in Figure 1. Moreover, Bader charges on N and two O atoms were obtained as 0.64 $|e|$ and 0.32 $|e|$, respectively. Derived parameters are consistent with the literature.[73,74]

To gain more insight into intramolecular N–O bonds, AIM-Bader, ICOHP, and ICOBI parameters were gathered and analyzed. According to Table 2, each bond is identical and shows a strong covalent character. For AIM-Bader parameters based on Table 1, $|V|/G$ and H/ρ parameters have values beyond transit type exceeding transit-covalent boundary in favor of covalency. For these bonds, potential energy density dominates.

Considering ICOHP and ICOBI values of each bond were measured to be −8.41 eV and 0.81, respectively. These values for N–O bonds are comparable with the C–C bond in diamond which has −9.6 eV for ICOHP and 0.95 for ICOBI, respectively.[68,75]

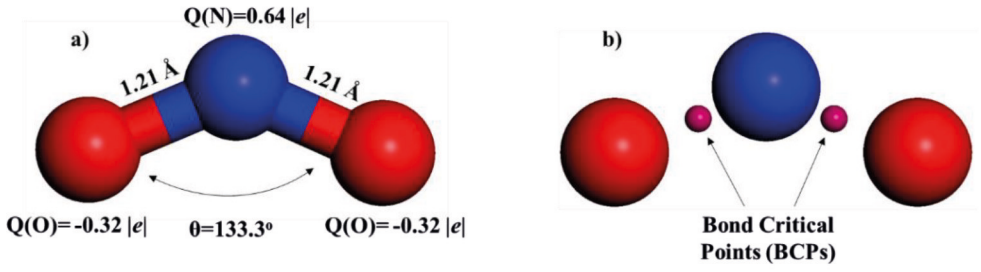

Figure 1. a) Optimized geometry of NO_2 molecule and Bader atomic charges, b) Bond critical points for each N–O bond. Nitrogen, oxygen atoms, and BCPs are shown in blue, red, and fuchsia colors, respectively.

Electronic, geometric and chemical bonding features of $M_nN_mO_n$/G layers

MnN_mO_n/G layers ($m+n=4$ *and* $1<m\leq 4$) created by following the procedure explained in the computational methods section and can be seen in Figure 2. Upon incorporation of oxygen atoms into porphyrin units, different motifs are formed. First oxygen can be substituted with any nitrogen atoms(Figure 2(b)) to create a MnN_3O layer. When two oxygen is incorporated, 3 different motifs are formed. In Figure 2(c), two oxygen atoms are the members of the same hexagon and are named MnN_2O_2 (hex). When they are positioned in opposite sites in Figure 2(d), the corresponding layer is named MnN_2O_2(opp).

In Figure 2(e), two oxygen atoms are the members of the pentagonal ring at the same time and are named MnN_2O_2(pent). Finally, three oxygen can be incorporated randomly into the porphyrin unit in Figure 2(f). The carbon atoms neighboring the porphyrin units can be classified as two types: C_P and C_H are the carbon atoms that are the members of the pentagonal and hexagonal rings, respectively, from Figure 1(a).

After ionic positions of six different N and O coordinated MnN_mO_n/G layers were updated, bond lengths in porphyrin units, Bader charges, magnetization per unit cell, and on Mn atom, formation energies, and the Mn binding energies are summarized in Table 3. First of all, the negative formation energies of all layers mean that oxygen substitution can be realized, however, the stability decreases as more oxygen is included in porphyrin units. Next, Mn binding energies on all layers prevent clustering threat except $MnNO_3$. Because the experimental bulk cohesive energy of Mn crystal is -2.92 eV and this value is higher than that of the Mn binding energy on $MnNO_3$, this layer might be deactivated due to a clustering problem.[35] Nevertheless, $MnNO_3$ layer is experimentally synthesized and worth to be investigated for NO_2 activation elaborately.[43,76]

Atomic distances between Mn and neighboring atoms in porphyrin units on MnN_mO_n/G layers were also updated upon O incorporation.[35] According to Table 3, it is seen that Mn–O distances get larger values than that of Mn–N. Accordingly, the distances between oxygen and neighboring carbon atoms are larger than that of nitrogen and carbon atoms. When these distance variations are evaluated together, the usage of oxygen atoms might considerably change the type of interactions in porphyrin units. This issue will be discussed later.

For the MnN_4 layer, Bader charge on Mn atom is measured to be $+1.32\ |e|$. When more oxygen atoms are included in porphyrin units, Mn atom holds more electrons and becomes more negative with reference to the MnN_4. Conformably, while atomic charges on O and N atoms in porphyrin units do not change dramatically, total charges on carbon moiety have significant variations. It means that the carbon moiety of the layers act as a main electron donor and plays a significant role in regulating Mn charges.[77,78] Lastly, MnN_mO_n/G layers have considerable magnetic character and Mn atom is the main source of the magnetization. MnN_4 layer has a 3.03 μ_B cell magnetization that is the parallel with the previous reports.[35,37] For the other layers, very high magnetization values have also been observed and the main contribution comes from the central Mn atom from Table 3.

To clarify the chemical bonding features of the layers upon oxygen incorporation, we resorted to AIM-Bader and COHP analyses. For this aim, Mn–N and Mn–O bonds in porphyrin units, the N–C and O–C bonds at the boundary between the carbon part and porphyrin unit have been taken into account. In Table S1, the averaged quantities over the number of the pair related to the interaction can be seen. For instance,

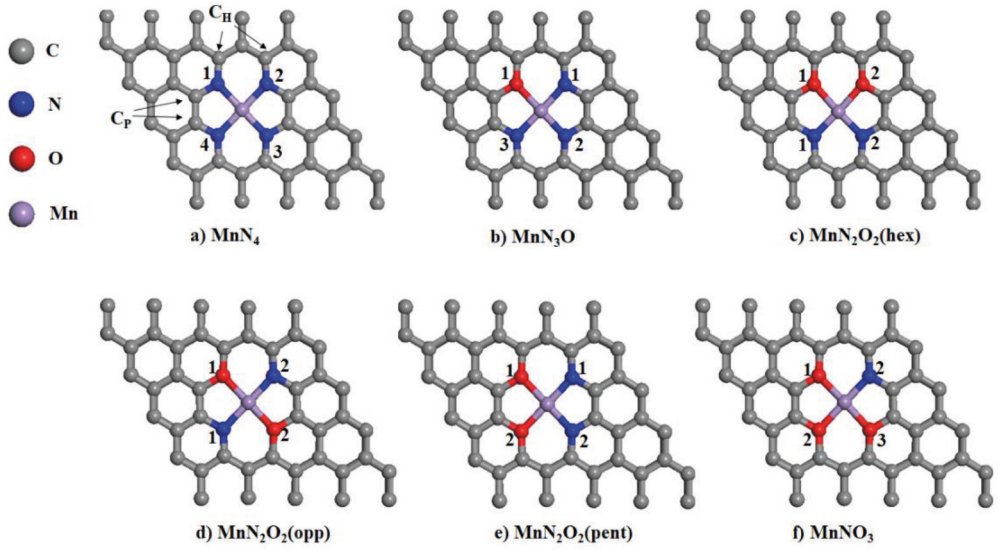

Figure 2. $M_nN_mO_n$/G ($m+n=4$ *and* $1<m\leq 4$) structures, a) MnN_4, b) MnN_3O, c) MnN_2O_2(hex), d) MnN_2O_2(opp), e) MnN_2O_2 (pent) and f) $MnNO_3$. Grey, blue, red, and purple spheres represent carbon, nitrogen, oxygen, and manganese atoms, respectively.

Table 3. From second to fifth columns show interatomic distances (d) in porphyrin units, formation energies(E_f), Bader atomic charges (Q), magnetization per unit cell and Mn atom (M), and binding energy (B.E.) of Mn atom to the porphyrin units. $\bar{Q}$ is the average charge on N or O atoms in porphyrin units. ΣQ(C) is the total charges on all carbon atoms on each layer. $\bar{d}$ is the average distance of N and O atoms to neighboring carbon atoms.

Layers	d (Å)	E_f (eV)	Q ($\|e\|$)	M (μ_B)	B.E. (eV)
MnN_4	Mn–N1 = 1.92 Mn–N2 = 1.92 Mn–N3 = 1.92 Mn–N4 = 1.92 $\bar{d}$(N–C) = 1.38	−3.19	Mn = +1.32 N1 = −1.24 N2 = −1.22 N3 = −1.23 N_4 = −1.15 $\bar{Q}$(N) = −1.21 ΣQ_C = +3.51	M_{tot} = 3.03 M_{Mn} = 2.46	−6.53
MnN_3O	Mn–N1 = 1.94 Mn–N2 = 1.88 Mn–N3 = 1.90 Mn–O1 = 1.98 $\bar{d}$(N–C) = 1.38 $\bar{d}$(O–C) = 1.43	−3.14	Mn = +1.26 N1 = −1.15 N2 = −1.22 N3 = −1.15 $\bar{Q}$(N) = −1.17 O = −1.15 ΣQ_C = +3.42	M_{tot} = 2.83 M_{Mn} = 2.31	−4.93
MnN_2O_2 (hex)	Mn–N1 = 1.86 Mn–N2 = 1.86 Mn–O1 = 1.99 Mn–O2 = 1.99 $\bar{d}$(N–C) = 1.38 $\bar{d}$(O–C) = 1.43	−3.05	Mn = +1.20 N1 = −1.15 N2 = −1.21 O1 = −1.13 O2 = −1.11 $\bar{Q}$(N) = 1.18 $\bar{Q}$(O) = 1.12 ΣQ_C = +3.42	M_{tot} = 2.70 M_{Mn} = 2.19	−3.44
MnN_2O_2 (pent)	Mn–N1 = 1.90 Mn–N2 = 1.90 Mn–O1 = 1.95 Mn–O2 = 1.95 $\bar{d}$(N–C) = 1.38 $\bar{d}$(O–C) = 1.43	−2.92	Mn = +1.19 N1 = −1.16 N2 = −1.24 O1 = −1.11 O2 = −1.11 $\bar{Q}$(N) = 1.20 $\bar{Q}$(O) = 1.11 ΣQ_C = +3.27	M_{tot} = 2.65 M_{Mn} = 2.17	−3.18
MnN_2O_2 (opp)	Mn–N1 = 1.91 Mn–N2 = 1.91 Mn–O1 = 1.94 Mn–O2 = 1.94 $\bar{d}$(N–C) = 1.38 $\bar{d}$(O–C) = 1.43	−2.91	Mn = +1.22 N1 = −1.13 N2 = −1.12 O1 = −1.12 O2 = −1.12 $\bar{Q}$(N) = 1.23 $\bar{Q}$(O) = 1.12 ΣQ_C = +3.27	M_{tot} = −2.72 M_{Mn} = −2.22	−3.15
$MnNO_3$	Mn–O1 = 1.92 Mn–O2 = 1.97 Mn–O3 = 1.95 Mn–N = 1.87 $\bar{d}$(N–C) = 1.38 $\bar{d}$(O–C) = 1.42	−2.67	Mn = +1.14 N1 = −1.11 O1 = −1.10 O2 = −1.12 O3 = −1.13 $\bar{Q}$(O) = 1.12 ΣQ_C = +3.32	M_{tot} = −2.68 M_{Mn} = −2.16	−1.56

because MnN_4 has four Mn–N bonds in porphyrin units, related parameters have been averaged over this number of bonds. As seen in Figure 2(a), carbon atoms which are part of the hexagonal and pentagonal rings were shown as C_H and C_P, respectively. To compare the chemical bonding features of the layers to each other, the MnN_4 layer was taken as a reference. Considering AIM-Bader parameters from Table S1 for the MnN_4 layer, it is seen that Mn–N bonds have an average value of 1.27 for $|V|/G$ parameter. Because the magnitude of the PED is larger than that of KED, the Mn–N bond has a transit character which has dual contributions from the ionic and covalent parts. Averaged over the 4 Mn–N bonds, H/ρ quantity is measured to be −0.36 and shows covalent character based on Table 1 suggested for AIM-Bader parameter intervals by Gatti.[59] Besides the type of bonding type elucidated from the parameter intervals, here, the effect of the oxygen incorporation will mainly be discussed. According to Table S1, it is clearly seen that oxygen substitution considerably changes AIM-Bader parameters.

For all oxygen-containing layer in porphyrin units, Mn–O and O–C (C_P and C_H) interaction always have less positive $|V|/G$ and less negative H/ρ values than that of N containing bonds. Based on Table 1, these bonds become more ionic. As a result, the variations on AIM-Bader parameters show that oxygen

substitution elevates the ionic character of the oxygen-containing bonds.

To support these findings based on AIM-Bader parameters, ICOHP and ICOBI parameters have also been considered for the same bonds. As shown in Table S1, average ICOHP and ICOBI values between four Mn–N were measured to be −2.69 eV and 0.22, respectively. These values show that Mn–N bonds in porphyrin units are mainly ionic. As more oxygen atoms are substituted into porphyrin units, Mn–N interactions regularly strengthen as opposed to that Mn–O. Table S1 clearly shows that Mn–O interactions are always weakening considering the average ICOHP values for Mn interactions with its neighboring atoms. Similar situations are also observed for oxygen and nitrogen interaction with neighboring carbon interactions. For the MnN_4 layer, N–C bonds have highly covalent character because of the significantly negative ICOHP values. In parallel with this, oxygen atoms have always weaker bonds with neighboring carbon atoms. To understand why oxygen-containing bonds are weaker than that of nitrogen, PDOS and −pCOHP plots should be interpreted together.

For the MnN_4 layer, PDOS curves (Figure 3a) contain various contributions. Around the fermi level, Mn, N, and C peaks are observed at the spin-down channel. While bonding orbitals are filled for Mn–N interactions, antibonding orbitals are mainly populated for N–C interaction around fermi level from the −pCOHP plot in Figure 3b. Around −3.3 eV, there is a significant N peak interacting with neighboring C atoms from PDOS curve. As opposed to the intuition taken by these peaks, these bonds at this energy regime are populated through their antibonding orbitals. From −4 eV to more negative energy values, N–C interactions are observed and interacting orbitals are populated through bonding orbitals. To screen the effect of the O incorporation into the layers, the $MnNO_3$ layer was selected. In Figure 4a, PDOS curves for various interactions on the $MnNO_3$ layer are seen. At first glance, some portion of the Mn(3d) states are filled which implies potential activity with respect to the MnN_4 layer. Around −0.5 eV and −0.8 eV regime below the fermi level, there are two peaks are appeared Mn–N–O and C atoms on both spin-down and spin-up channels, respectively. Among these interactions, the antibonding orbitals between oxygen and neighboring carbon atoms populated can be seen by cyan colored line in Figure 4b. Below the fermi level, C(2p) and O(2p) states are more visible than that of Mn(3d) and N(2p). Interestingly, Mn(3d) sharp spin-down peak at −2 eV is seen, however, it is not part of any obvious interaction with any surrounding atom. Considering

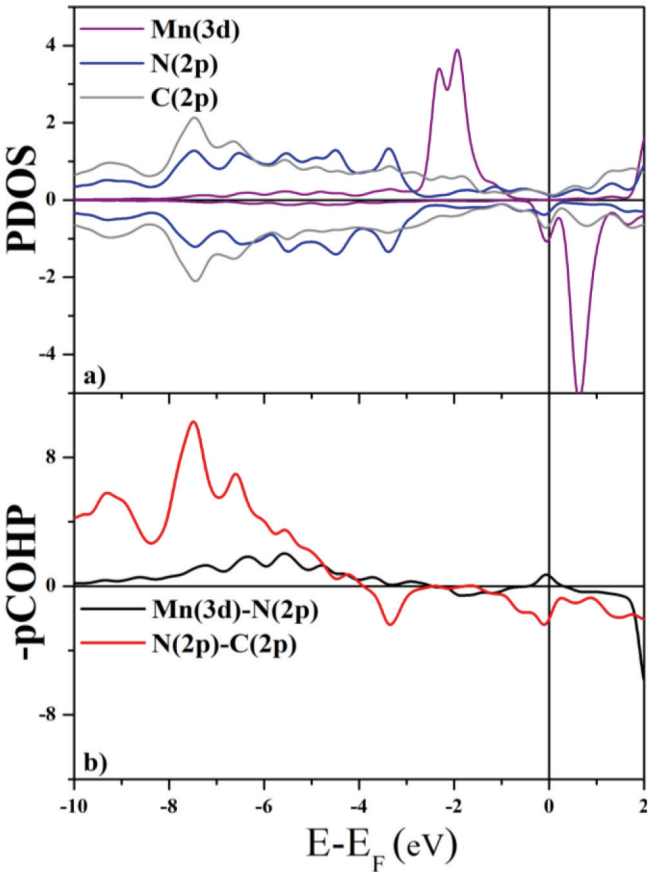

Figure 3. a) PDOS plots for Mn and N interactions in porphyrin units. Purple, blue, and grey lines are showing the electron population at different energies for 3d orbital of Mn, 2p orbitals of N, and 2p orbitals of C atoms, respectively. b) Black and red curves show the orbital projected COHP plots (positive(negative) sign indicates bonding(anti-bonding) character) for Mn–N and N–C interactions including both C_H and C_P atoms, respectively.

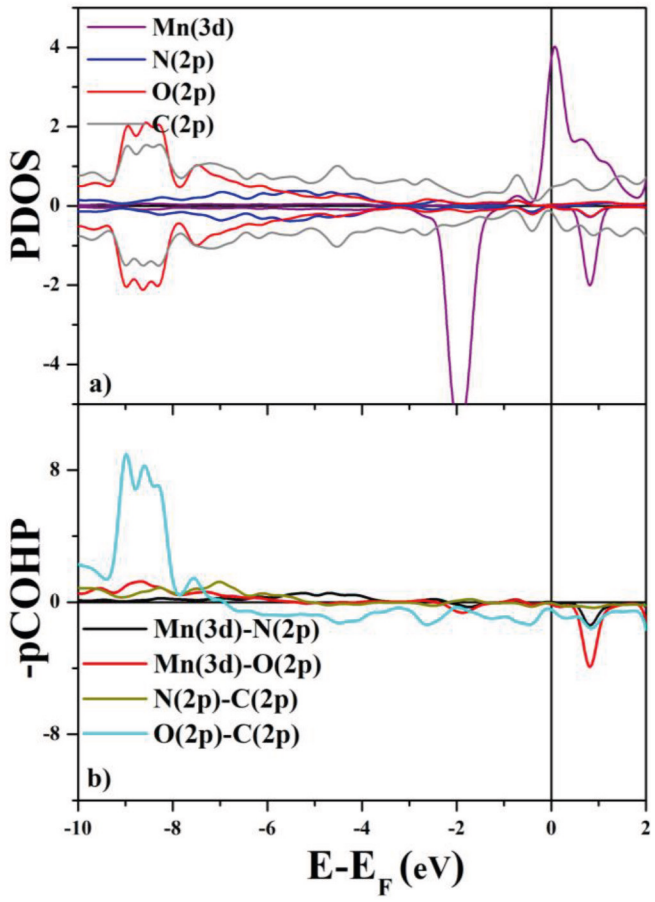

Figure 4. a) PDOS plots for Mn, N, O, and C interactions on $MnNO_3$. Purple, blue, grey, and red lines are showing the partial electron population over the energy interval for 3d orbital of Mn, 2p orbitals of N, O, and C atoms, respectively. b) Black, red, dark yellow, and cyan curves show the orbital projected COHP plots (positive(negative) sign indicates bonding(anti-bonding) character) for Mn–N and Mn–O, N–C and O–C interactions including both C_H and C_P atoms, respectively.

the –pCOHP plot for $MnNO_3$ in Figure 4b, oxygen, and carbon antibonding orbitals are filled while bonding orbitals between nitrogen and carbon atoms are less populated with reference to the MnN_4 case in Figure 3b. In addition, N(2p)–C(2p) antibonding orbitals are less populated while bonding orbitals are more populated on MnN_4 in Figure 3b. This case is reversed on the $MnNO_3$ layer for O(2p)–C(2p) bonds. For other layers which are MnN_3O, MnN_2O_2(hex), MnN_2O_2(opp), and MnN_2O_2(pent), PDOS and –pCOHP curves can be seen in Figure S2–S5. On these layers, Mn(3d) states become partially filled as more oxygen atoms are substituted with N atoms in porphyrin units.

The interaction between neighboring carbon atoms and oxygen atoms becomes more visible as more oxygen the layer have, restricted to a certain energy range and weaker than that of N–C with reference to the MnN_4 (Figure S1–S4). This is why the stability of the layers decreases as more oxygen is incorporated into the layers. This means that the substitution of more electronegative element into porphyrin units weakens the chemical bonds, these chemical bonds become more ionic and the activity of the Mn atom is regulated through updating d-orbital electron distribution.[37,77,78]

Electronic, geometric and chemical bonding features NO_2 adsorption on MnN_mO_n/G layers

To investigate NO_2 adsorption on the MnN_mO_n/G layer, the most stable geometries of NO_2 molecule from oxygen (O-side configurations in Figure 5) and nitrogen (N-side configurations in Figure S6) atoms have been found through geometric optimizations. In Table 4, adsorption energies via oxygen atoms (O-side) on all layers have lower values than that of nitrogen atoms (N-side) configurations (given in parenthesis). Because of that, only O-side adsorption configurations will be considered in the remaining subchapters. On MnN_4/G and MnN_3O/G layers, NO_2 is adsorbed via one oxygen atom which is in contrast with the literature[31] (Figure 5a and 5b). During the adsorption process on these layers, adsorption energies are −1.41 and −1.50 eV, and the bond lengths between nitrogen and Mn-bounding oxygen atoms are elongated to 1.32 and 1.33 Å for MnN_4 and MnN_3O, respectively. Another bond in the molecule remains inactivated with reference to the gas phase in Figure 1.

Adsorption configurations of the NO_2 molecule on MnN_2O_2(hex), MnN_2O_2(opp), MnN_2O_2(pent) and $MnNO_3$ layers are similar to each other in Figure 5c–5f, NO_2 molecule is activated via its two N–O bonds as opposed to the case on MnN_4 and MnN_3O layers. During the adsorption of NO_2, the two bond lengths between Mn and O atoms equally elongate on each layer from Table 4. The largest bond elongation is screened as 1.31 Å on MnN_2O_2(hex) layer for each N–O bond. Intramolecular N–O bond lengths are measured nearly the same within each of the remaining layers. Interestingly, even if MnN_2O_2(hex) layer has adsorption energy in the midst at the range of all, the largest elongation occurs on this.

The largest adsorption energy is observed on $MnNO_3$/G layer which is one of the largest adsorption energy calculated based on single atom embedded catalytic systems so far.[1] These findings show that oxygen incorporation into the porphyrin unit of MnN_4 layer in different numbers and combinations greatly enhances the adsorption capability of NO_2 molecule.

To gain some insight for charge transfer between molecule-porphyrin unit-carbon moiety of the layers, Bader atomic charges and related plots for Electron Density Differences (EDD) might be useful. According to Figure 6, it is obvious that electron depletion is observed on N–O bonds in the molecule seen by the cyan color. Simultaneously, electrons are accumulated on the atoms in the NO_2 molecule seen by the yellow color. This clarifies that the electron transfer process is bidirectional over the bonding-antibonding orbitals of the NO_2 molecule which obeys the donation-back donation rule.[79,80]

As clearly seen from Table 4 and Figure 6, a varying amount of net charges are transferred to the NO_2 molecule. The most significant amount of electron transfer by $-0.82\ |e|$ occurs on MnN_2O_2(hex) layer. Based on Table 4 and Figure 6, a deeper analysis should be made using Bader charges and electron

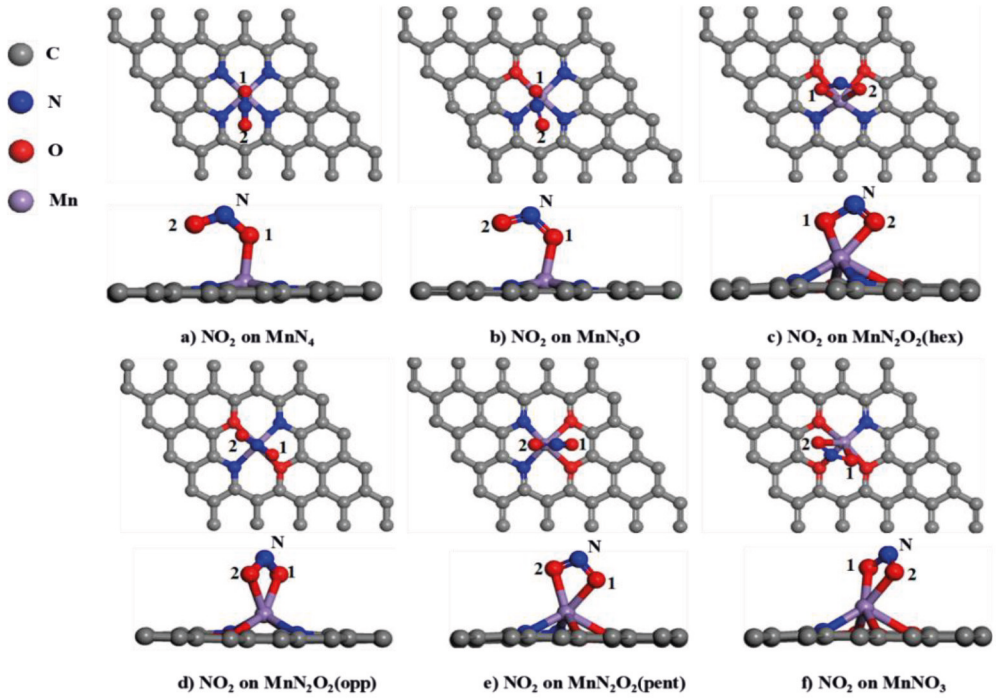

Figure 5. NO_2 molecule from O-site on a) MnN_4, b) MnN_3O, c) MnN_2O_2(hex), d) MnN_2O_2(opp), e) MnN_2O_2(pent) and f) $MnNO_3$ layers. Grey, blue, red, and purple spheres represent carbon, nitrogen, oxygen, and manganese atoms, respectively.

Table 4. d is the interatomic distances in the adsorbed molecule and between Mn and the atoms in the molecule, total Bader atomic charges on the molecule, Mn atom, total N and O charges on porphyrin units, and total charges of carbon moiety on each layer (Q), magnetization per unit-cell after adsorption (M_{cell}) and Mn atom (M) and binding energy (B.E.) of Mn atom to the porphyrin units. In E_{ads} column, the adsorption energies of the NO_2 molecule from the N-side in parenthesis. In ΣQ(Mn) column, the change in the Mn atomic charges with reference to the bare layers as defined as $Q_{Mn\text{-}ads}-Q_{Mn\text{-}layer}$.

NO_2 adsorbed layers	d (Å)	E_{ads} (eV)	ΣQ (NO_2)	ΣQ (Mn)	ΣQ(N + O) in porp.	ΣQ(C)	$\Sigma M_{cell}(\mu_B)$
MnN_4	Mn–O1 = 2.01 Nm–O1 = 1.32 Nm–O2 = 1.22	−1.41 (−1.35)	−0.59	1.52 (0.20)	−4.68	3.74	−2.70
MnN_3O	Mn–O1 = 1.97 Nm–O1 = 1.33 Nm–O2 = 1.22	−1.50 (−1.42)	−0.61	1.46 (0.21)	−4.56	3.71	2.66
MnN_2O_2 (hex)	Mn–O1 = 1.98 Mn–O2 = 1.98 Nm–O1 = 1.31 Nm–O2 = 1.31	−2.26 (1.74)	−0.82	1.45 (0.25)	−4.52	3.89	−3.30
MnN_2O_2 (pent)	Mn–O1 = 2.04 Mn–O2 = 2.04 Nm–O1 = 1.30 Nm–O2 = 1.30	−2.39 (−1.88)	−0.80	1.46 (0.27)	−4.50	3.84	−3.81
MnN_2O_2 (opp)	Mn–O1 = 2.13 Mn–O2 = 2.13 Nm–O1 = 1.29 Nm–O2 = 1.29	−2.18 (−1.71)	−0.77	1.47 (0.25)	−4.48	3.78	−4.60
$MnNO_3$	Mn–O1 = 2.11 Mn–O2 = 2.11 Nm–O1 = 1.30 Nm–O2 = 1.30	−2.86 (−2.53)	−0.75	1.43 (0.29)	−4.52	3.84	−4.67

density differences belonging to the participation of different parts of the layers after adsorption. On the MnN_4 layer (Figure 6a), N atoms in the porphyrin unit behave like an electron provider for the adsorption which can be recognized

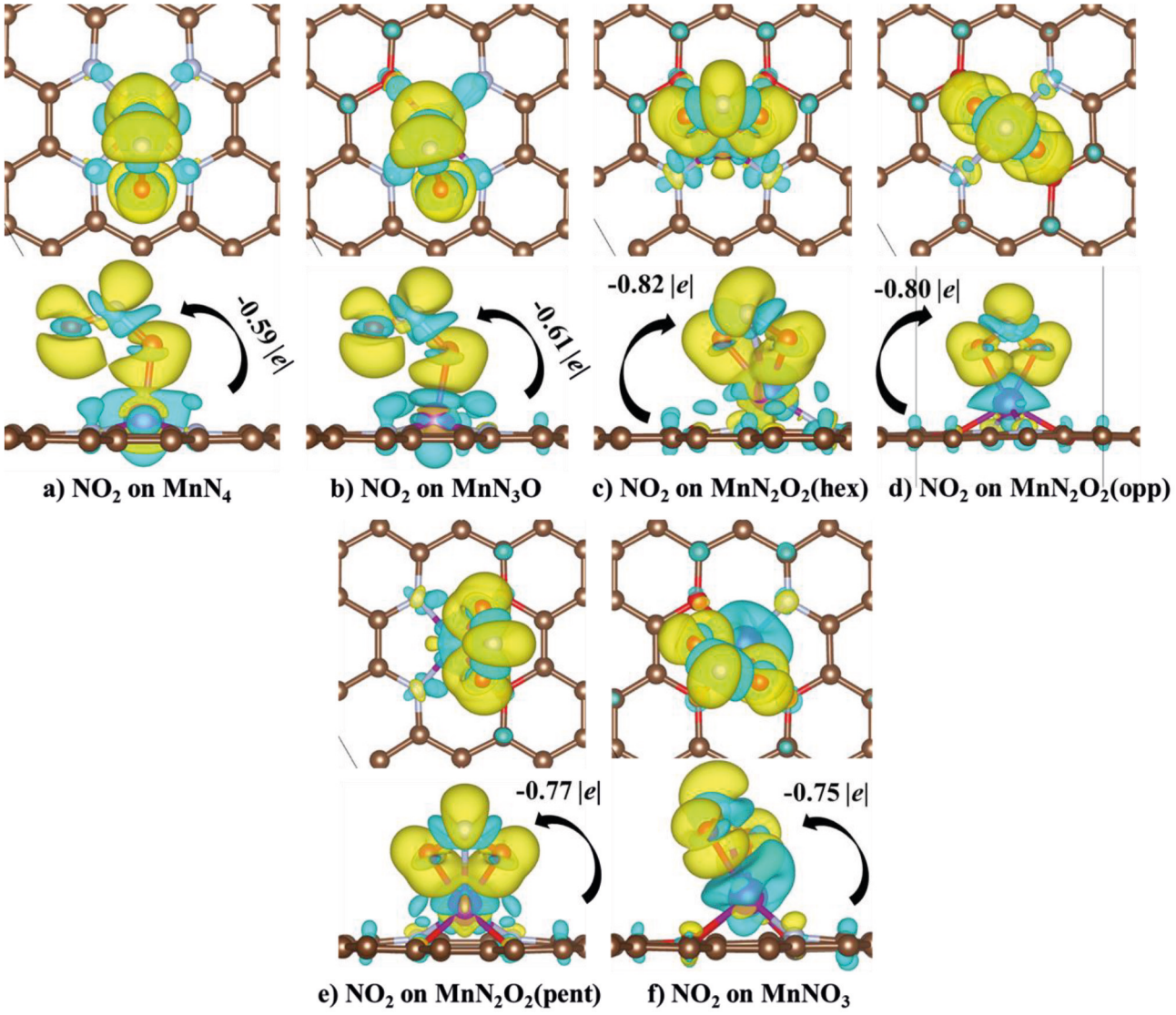

Figure 6. Electron density differences (EDD) plots for NO_2 adsorption a) MnN_4, b) MnN_3O, c) MnN_2O_2(hex), d) MnN_2O_2(opp), e) MnN_2O_2(pent) and f) $MnNO_3$ layers. Yellow and cyan colors represent electron accumulation and depletion in space, respectively. The isosurface value is 0.0017 $e/Bohr^{-3}$.

from the cyan-colored local electron densities. Moreover, electron densities between O atoms in the molecule and Mn overlap one another which elucidates that the Mn atom is the sole active site in the porphyrin unit. This observation is valid for all layers during NO_2 adsorption. Additionally, there is no apparent electron contribution from specific carbon atoms to the porphyrin unit and the NO_2 molecule. In this case, the total charges of nitrogen atoms on the porphyrin unit, carbon moiety, Mn, and molecule are measured as $-4.68\ |e|$, $3.74\ |e|$, $1.52\ |e|$ and $-0.59\ |e|$, respectively. When oxygen-incorporated layers are taken into account, the first striking observation is that the neighboring carbon atoms to the oxygen atom(s) in the porphyrin units lose(s) more electrons than that of nitrogen atoms. This is more obvious for MnN_3O, MnN_2O_2(hex) and MnN_2O_2(opp) layers where all (here two) nearby carbon atoms are injecting their electrons much more obviously than the others. From these findings, it can be comprehended that oxygen atoms in specific porphyrin configurations make electron transfer easier than that of nitrogen atoms. The most significant electron transfer to the NO_2 occurs on MnN_2O_2 (hex) layer by $-0.82\ |e|$. Here, total carbon atomic charges are measured to be $3.89\ |e|$. To assess the direction of the charge transfer from carbon atoms to any part, an elaborate analysis should be made. In Table 4, the total charges of the carbon atoms and total atomic charges in porphyrin units (N and O atoms if exist) except Mn are always positive and negative, respectively. When oxygen-incorporated layers are considered, carbons become more positively charged. Simultaneously, total atomic charges in porphyrin units except Mn lose some of their electrons and do not change significantly. This finding states that carbon atoms are not responsible for the varying nitrogen and oxygen atomic charges in porphyrin units. The lost

electrons from the carbon part are probably transferred to the molecule. As a result, the carbon part of the layers behaves like an electron reservoir.

In order to get deeper insight regarding some selected interactions in the adsorbed configurations, PDOS and −pCOHP curves can be interpreted simultaneously to understand which porphyrin configuration weakens N–O bonds the most in the molecule. To analyze the effect of the active site upon adsorption, MnN_4 is selected and will be used for benchmarking. All atomic indices can be followed from Figure 5. In Figure 5a, one of two N–O bonds in the molecule is activated because adsorption is realized through one Mn–O pair. From PDOS in Figure 7, Mn(3d)–O1(2p) interaction is obvious around −1.8 eV at the spin-up channel. At this energy value, the peak heights of the cyan and dark yellow curves belonging to N and O2 atoms in the molecule, respectively, are comparable to each other. They are relatively stronger bond with reference to the N–O1 and remains unchanged. In spin down-channel, there are

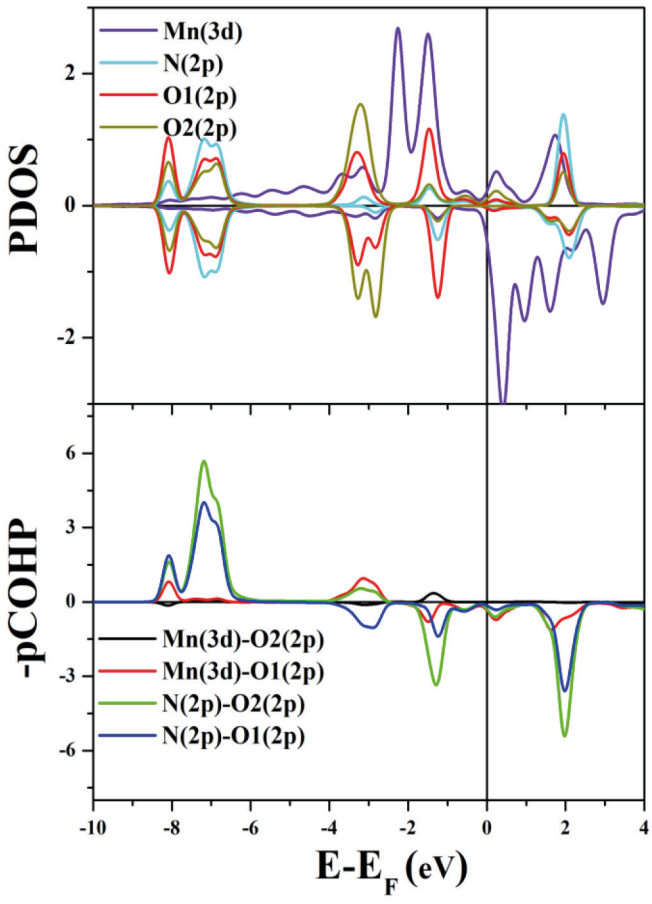

Figure 7. PDOS and −pCOHP curves for NO_2 adsorption on the MnN_4 layer. For PDOS curves, Mn(3d), N(2p), O1(2p), and O2(2p) orbitals are shown by purple, cyan, red, and dark yellow colored lines, respectively. For −pCOHP curves, electron populations on bonding, non-bonding, and antibonding orbitals for Mn(3d)–O2(2p), Mn(3d)–O1(2p), N(2p)–O2(2p) and N(2p)–O1(2p) interactions are shown by black, red, green and blue colored straight lines. Atomic indices can be followed from Figure 5.

some other fundamental interactions for NO_2 adsorption on the MnN_4 layer. On this layer, only a single bond is activated.

From −pCOHP curves, the black curve is indicating that Mn–O2 (farthest oxygen) interaction is mainly non-bonding because non-zero values span all over the valence band. Moreover, some of the electrons populate Mn–O1 antibonding orbitals at −1.8 eV can be seen by the red curve. The most interesting issue here are belonging to the intramolecular bonds. The green lines of −pCOHP part in Figure 7 illustrate the N–O2 interactions in the molecule in which the electrons are accumulated in bonding and antibonding orbitals at −1.6 and −3.1 eV, respectively. While the peak at −1.6 eV has an anti-bonding character, the other peak at −3.1 eV has a bonding character. Considering N–O1 interaction, only anti-bonding orbitals are populated by transferred electrons from the carbon moiety up to the −4 eV below the fermi level. The mechanism of the N–O1 bond weakening can also be understood by the combinatorial interpretation of AIM-Bader parameters along with the ICOHP and ICOBI values. BCPs can be seen in Figure S7. Based on AIM-Bader parameters in parallel with Table 2, N–O2 remains unchanged with reference to the gas phase in terms of $|V|/_G$ and H/ρ parameters. However, the N–O1 bond which is elongated to 1.32 Å from 1.22 Å is weakened and falls into the transit type bond range based on H/ρ parameter where the ionic and covalent parts are simultaneously responsible with varying rates. Even if this bond is still covalent for $|V|/_G$ parameter, the bond is weakened and the ionic contribution is increased. From ICOHP and ICOBI values, the same conclusion is reached. Similar to the change in AIM-Bader parameter trends, ICOHP values are measured to be −13.56 eV and −16.86 eV for elongated N–O1 and unaltered N–O2 bonds, respectively. This finding implies that the N–O1 bond is weakened by populating antibonding orbitals. Moreover, ICOBI value for the elongated N–O1 bond in the molecule is 0.65 which means the increasing ionic character of this bond with reference to the gas phase value in Table 2. Considering the Mn–O1 bond, $|V|/_G$ and H/ρ parameters have 1.21 and −0.26 values which show the transit type of the bond. ICOHP and ICOBI values for this bond indicates ionicity and are equal to −2.13 eV and −0.14, respectively. Similar to MnN_4, only a single N–O bond in the molecule is activated on the MnN_3O layer. AIM-Bader, ICOHP, and ICOBI parameters are changed slightly among these layers can be seen in Table S2. Because AIM-Bader, ICOHP, and ICOBI parameters belonging to intramolecular bonds and adsorption geometry are nearly the same as that of MnN_4, Mn–O1 interaction strength based on these parameters might be useful to create a correlation. It is quite apparent that the covalent contribution of the Mn–O1 bond is increasing based on these $|V|/_G$, H/ρ, ICOHP and ICOBI parameters and adsorption energies of NO_2 molecule were calculated as −1.41 and −1.50 eV for MnN_4 and MnN_3O layers, respectively.

Considering the adsorption configurations on the MnN_2O_2(hex), MnN_2O_2(opp), MnN_2O_2(pent) and $MnNO_3$ layers, the NO_2 molecule is activated via both N–O intramolecular

bonds. Intramolecular N–O1/O2 bond lengths and Mn–O1/O2 distances are all the same in each of two or more oxygen-containing layers in the porphyrin unit in Table 4. This finding indicates that N–O1/O2 bonds are activated evenly. AIM-Bader, ICOHP, and ICOBI parameter values also support this idea. According to Table S2, $|V|/_G$ and H/ρ values have been noticeably decreased in comparison with the gas phase. However these values for the layers where two bonds are activated are slightly higher than that of MnN_4 and MnN_3O layers with reference to elongated N–O1 bonds. Nevertheless, it should not be dismissed that two bonds are activated instead of one. The same trend is observed for ICOHP and ICOBI parameters. The most striking result for N–O bond activation, the MnN_2O_2(hex) layer is the most active layer.

On this layer, $|V|/_G$ and H/ρ parameters get the value of 2.41 and −1.74, respectively. ICOHP and ICOBI values have the smallest values on all two or more oxygen-incorporated layers which are −14.25 eV and 0.70, respectively. It is quite interesting that even if the NO_2 adsorption energy is moderate among all layers, the largest activation occurs. To gain more insight into the activation mechanism, PDOS and –pCOHP curves should be interpreted together. According to the PDOS part of Figure 8, 2p orbitals N, O1, and O2 atoms are interacting at the spin-down channel. However, the corresponding peak at the same energy in –pCOHP curve indicates that this interaction is antibonding and weakens the N–O1 and N–O2 bonds, simultaneously. In PDOS plot, Mn is interacting with the oxygen atoms of the molecule between −2.7 and −3.8 eV below the fermi level. Based on –pCOHP plot, these interactions are bonding from the dashed black and red curves. To get deeper insight, AIM-Bader, ICOHP, and ICOBI parameters might be useful to identify bond types. In the row belonging to the $MnN_2O_2(hex)$ layer in Table S2, $|V|/_G$ and H/ρ parameters are measured as −2.41 and 1.74, implying covalent and transit bond type, respectively. In addition, ICOHP and ICOBI parameters have values of −14.25 eV and 0.70, respectively, which are the smallest values measured for these bonds on all layers. This means that MnN_2O_2(hex) layer activates the intramolecular N–O bonds the most among all layers. Considering Mn–O1/O2 interactions, bonding types are transit where the covalent and ionic are mixed at different rates based on $|V|/_G$ and H/ρ. However, ionicity dominates because these values are closer to the ionic limit in the parameter intervals. The same bond types are observed via ICOHP and COBI parameters for the same bonds. Mn–O1 and Mn–O2 bond types are mainly ionic because of relatively closer values of the ICOHP and ICOBI to zero. When the other layers are taken into account, N–O bond activation abilities are seen as relatively closer to that of MnN_2O_2(hex) layer. Related PDOS and – –pCOHP plots are illustrated in Figures S8–S12.

Finally, the magnetic characteristics of the NO_2 adsorbed layers should be discussed with reference to the bare layers. In order to compare bare and adsorbed layers, one should take into account magnetization per unit cell ($M_{cell}(\mu_B)$) in Table 5. In the last column of Table 5, ΔM_{cell} corresponds to the magnetization difference between before and after adsorption given by Equation 4:

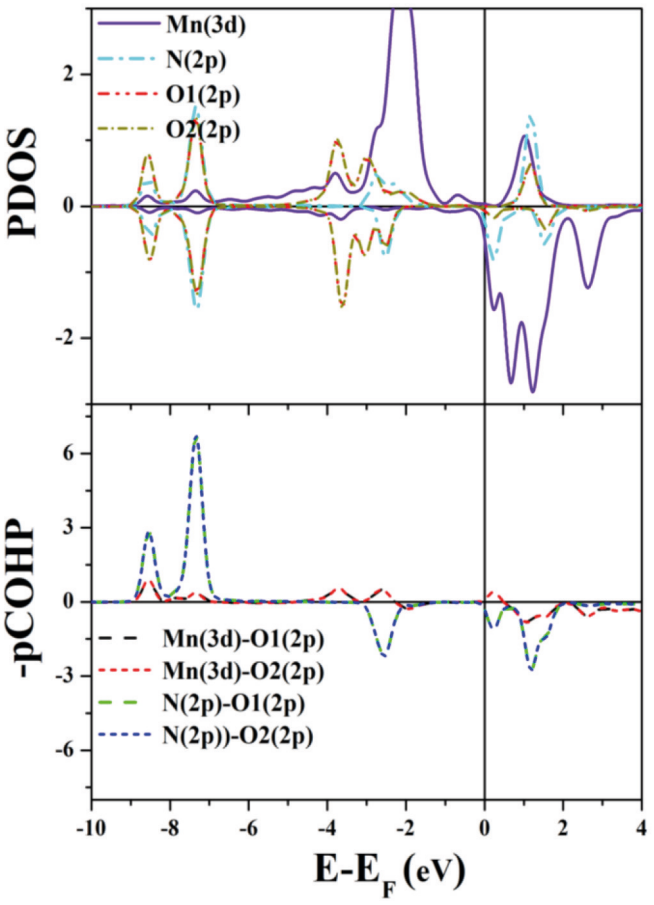

Figure 8. PDOS and –pCOHP curves for NO_2 adsorption on MnN_2O_2(hex) layer. For PDOS curves, Mn(3d), N(2p), O1(2p), and O2(2p) orbitals are shown by straight purple, dashed cyan, dashed red, and dashed dark yellow colored lines, respectively. For –pCOHP curves, electron populations on bonding, non-bonding, and antibonding orbitals for Mn(3d)–O1(2p), Mn(3d)–O2(2p), N(2p)–O1(2p) and N(2p)–O2(2p) interactions are shown by dashed black, dashed red, dashed green and dashed blue colored lines. Atomic indices can be followed from Figure 5.

Table 5. Magnetization per unit cell before and after NO_2 adsorption on all layers. In the last column, the variation of the magnetization can be seen.

Layers	$M_{cell}(\mu_B)$ (Before Ads.)	$M_{cell}(\mu_B)$ (After Ads.)	$\Delta M_{cell}(\mu_B)$
MnN_4	3.03	−2.70	5.73
MnN_3O	2.83	2.66	0.17
MnN_2O_2 (hex)	2.70	−3.30	6.00
MnN_2O_2 (pent)	2.65	−3.81	6.46
MnN_2O_2 (opp)	−2.72	−4.60	1.88
$MnNO_3$	−2.68	−4.67	1.99

$$\Delta M = M_{Bef.\ Ads.} - M_{Aft.\ Ads.} \quad (4)$$

The first and second terms stand for the magnetization per unit cell before and after adsorption, respectively.

According to our results, variation in magnetization is greatly affected by NO_2 adsorption. When this quantity is taken into consideration, it varies from $+6$ μ_B to 0.17 μ_B meaning remarkable modulation of magnetic properties. Finally, this wide magnetization change proposes the usage of these layers for spintronic applications.[28]

Correlations including AIM-Bader and ICOHP/ICOBI parameters

In Bader partitioning scheme, the three-dimensional electron density is divided into subspaces and charge density gets its maximum at the nucleus positions.[81] The tail of the electron density exponentially decays between atoms and creates zero-flux surfaces which characterize bonds.[82] In COHP analysis, the plane wave function is converted to the wave function which is a conversion of the molecular orbitals to the bonding/antibonding fragments. Even if AIM-Bader and COHP/COBI formalism are different from each other, some correlations have been captured for the bare layers and adsorbed configurations, separately.

The first interesting correlation is clarifying the relation between the formation energies of the layers and ICOHP values of the Mn with the neighboring atoms seen in Figure 9a. Related data can be found in Table 3 and Table S1. As explained before, oxygen incorporation mitigates the bond strength in porphyrin units on the related layers. In parallel with this, the formation energies are decreasing meaning oxygen incorporation becomes easier as more oxygen is substituted with nitrogen atoms.

A second remarkable correlation for bare layers arises between ICOBI and Mn partial Bader charges in Figure 9b. Based on Table 3 for Mn atomic charges, Mn atom becomes less positive meaning that more electrons are transferred to it as more oxygen is replaced in porphyrin units. In the previous discussions and CDD plots, carbon atoms donate their electrons mainly to Mn atoms through oxygen atoms. Shortly, oxygen incorporation makes porphyrin units more ionic. In this perspective, total ICOBI values of the bonds between Mn and its neighbors follow the same trend as the Mn charges.

In Figures 10a and 10b, the correlation between ICOHP and H/rho; ICOBI, and $|V|/K$ are represented, respectively. The pairs have been selected based on their units. ICOHP and ICOBI quantities are well in a linear relationship with H/rho and $|V|/K$, respectively. Our results indicate that Bader charge partitioning is very successful to determine bond types on MnN_mO_n/G layers. Moreover, COHP and ICOBI parameters which are orbital-based bond energies and Wiberg-Mayer based bond index are very efficient to depict bond weakening and bond types in correlation with AIM-Bader parameters.

When taking into consideration intramolecular N–O bonds in adsorbed NO_2 molecules, the linear correlation amongst ICOHP–H/rho and ICOBI-$|V|/K$ quantities are observed. According to Figures 11a and 11b, N–O bond weakening and resulting bond type are measured via the relation of the considered quantities. Moreover, the formation energies of the layers have an inverse correlation with the NO_2 adsorption energies. Based on Figure 10c, as more oxygen atoms are incorporated into porphyrin units, NO_2 adsorption energy increases. In this context, MnN_4 has the smallest adsorption energy while the $MnNO_3$ layer has the largest. This might be occurred because of

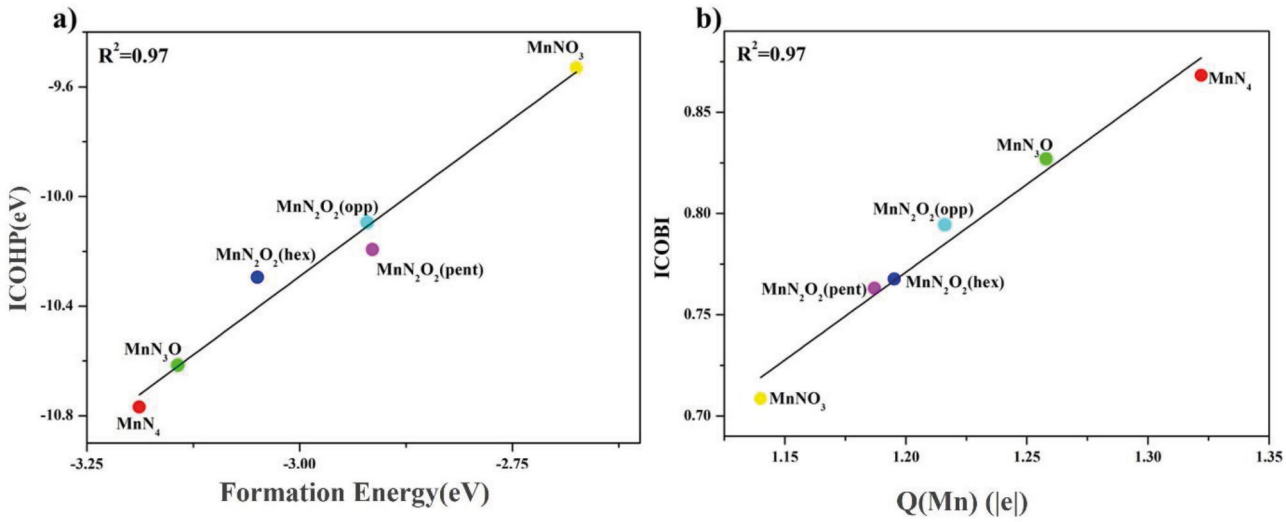

Figure 9. a) Correlation between ICOHP and formation energies of the layers. ICOHP is gathered from the bonds between Mn and neighboring atoms. Both quantities are in eV units. b) Correlation between ICOBI and Mn Bader partial atomic charges. ICOBI is gathered from the bonds between Mn and neighboring atoms. ICOBI is unitless and Q(Mn) has the unit of $|e|$.

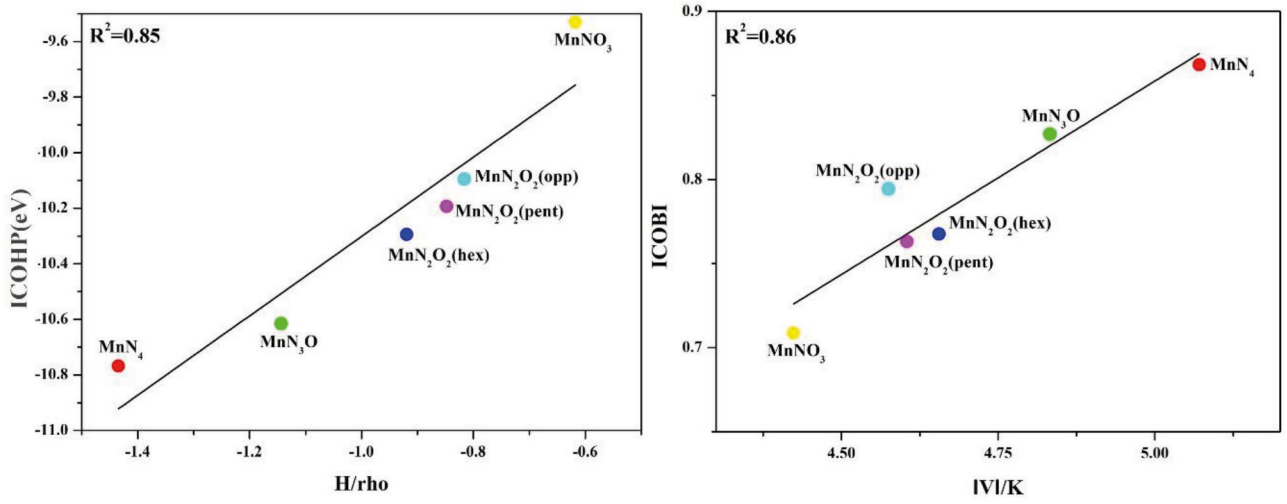

Figure 10. a) Correlation between ICOHP and H/rho of the layers. ICOHP and H/rho quantities are gathered from the bonds between Mn and neighboring atoms. ICOHP is in eV, H/rho is in atomic units. b) Correlation between ICOBI and |V|/K which are both unitless. Data is gathered in the same way as that of ICOHP and H/rho quantities.

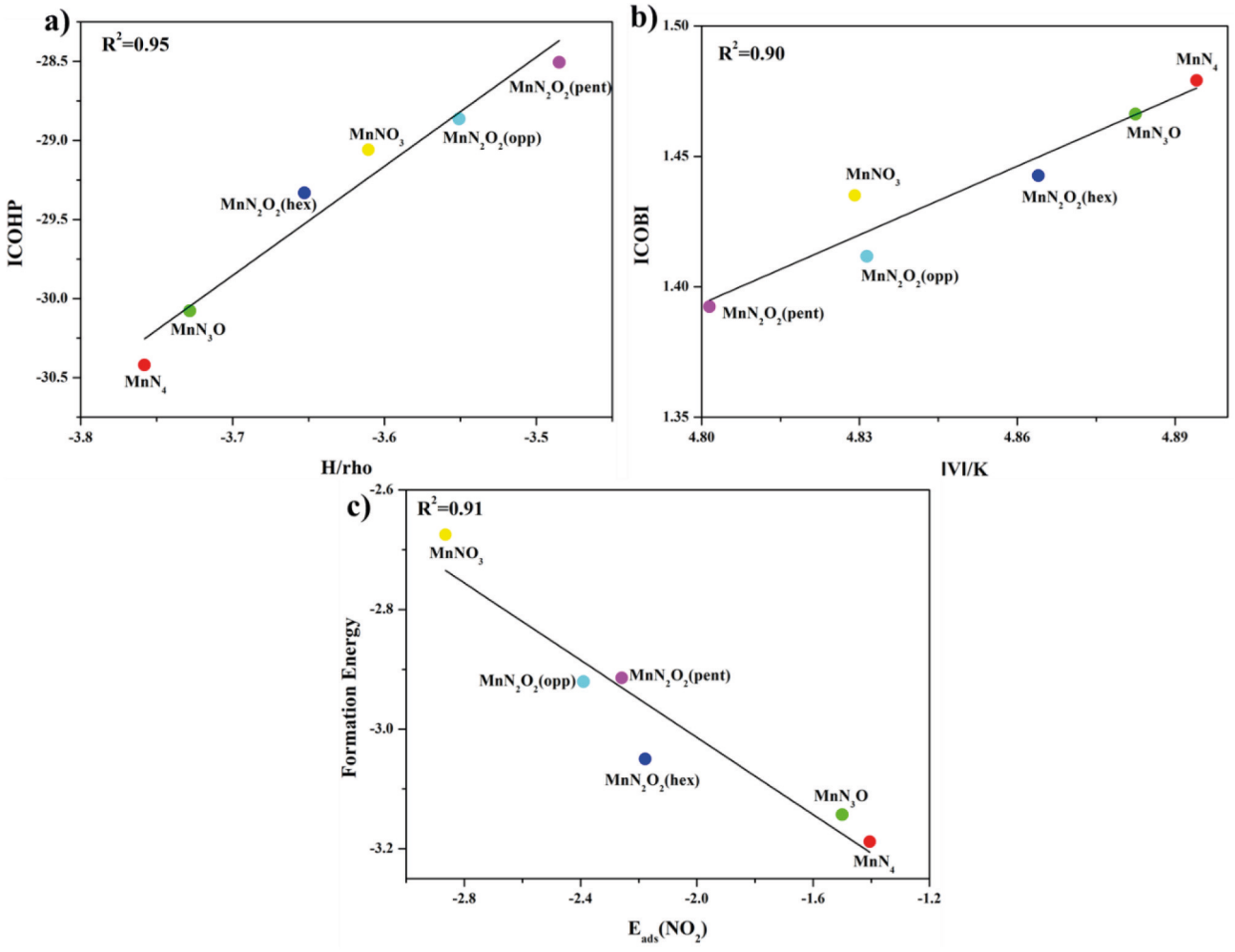

Figure 11. a) Relationship between total ICOHP and total H/rho of the intramolecular N–O bonds. ICOHP is in eV, H/rho is in atomic units. b) Relationship between total ICOBI and total |V|/K of the intramolecular N–O bonds. Both quantities are unitless. c) Relationship between layer formation energies and NO_2 adsorption energies. Both terms are in eV units.

the electronic modulation of the Mn atom at the center of the porphyrin units.

Conclusion

In this article, oxygen incorporated the MnN_4 layer (and its derivatives) and its activation capability over NO_2 molecule have been investigated. The preliminary results regarding the formation of the layers showed that oxygen substitution with the nitrogen atoms changes bonding types to be more ionic between Mn and neighboring atoms. Resulting interactions have been observed to be more ionic. This finding has been supported by the variation of the AIM-Bader and ICOHP/ICOBI parameters. Moreover, oxygen atoms were looked to be efficient charge transmitters with reference to the nitrogen atoms in porphyrin units clarified by EDD plots. After NO_2 adsorption, one of two bonds is activated on MnN_4 and MnN_3O layers. The remaining layers activate both intramolecular N–O bonds. The changes in the bonding types in porphyrin moieties in bare layers and intramolecular N–O bonds have been investigated also by AIM-Bader and ICOHP/ICOBI parameters. The variation in these parameters showed that MnN_2O_2(hex) layer is the most active one over the NO_2 molecule. For all weakened bonds, antibonding orbitals are populated to some extent confirmed by –pCOHP curves along with the PDOS.

The relation between AIM-Bader and ICOHP/ICOBI parameters was observed for the bonds which have a descriptive capability. We have found that AIM-Bader and ICOHP/ICOBI parameters follow the same trend overwhelmingly. Finally, formation energies were measured to have a close relationship with NO_2 adsorption energies which indicates that oxygen incorporation modulates the electronic structure of the Mn atom as an active site. These research outputs state that AIM-Bader parameters describe the bond types variation trends mentioned above such as ICOBI and ICOHP even if they are generated through different theoretical foundations.

Acknowledgment

The numerical calculations reported in this paper were fully/partially performed at TUBITAK ULAKBIM, High Performance and Grid Computing Center (TRUBA resources).

Conflict of Interest

The authors declare no conflict of interest.

Data Availability Statement

The data that support the findings of this study are available in the supplementary material of this article.

Keywords: Bader topological analysis · crystal orbital bond index (COBI) · crystal orbital Hamilton population (COHP) · nitrogen dioxide activation · small molecule activation

[1] H. Cruz-Martínez, H. Rojas-Chávez, F. Montejo-Alvaro, Y. A. Peña-Castañeda, P. T. Matadamas-Ortiz, D. I. Medina, *Sensors* **2021**, *21*, 1992.
[2] I. Manisalidis, E. Stavropoulou, A. Stavropoulos, E. Bezirtzoglou, *Frontiers in public health* **2020**, 14.
[3] Y. S. Najjar, *Innovative energy policies* **2011**, *1*, 1–9.
[4] R. G. Zhu, H. Y. Xiao, Z. Wen, Y. Zhu, X. Fang, Y. Pan, Z. Chen, H. Xiao, *Journal of Geophysical Research: Atmospheres* **2021**, *126*, e2021JD034741.
[5] W. H. Organization. Review of evidence on health aspects of air pollution: REVIHAAP project: technical report. World Health Organization. Regional Office for Europe; **2021**.
[6] G. Li, K. Shen, L. Wang, Y. Zhang, H. Yang, P. Wu, B. Wang, S. Zhang, *Appl. Catal. B* **2021**, *286*, 119865.
[7] Y. Liu, Y. You, Z. Li, X. Yang, X. Wu, C. Zhao, Y. Xing, R. T. Yang, *J. Hazard. Mater.* **2021**, *407*, 124380.
[8] J. Li, X. Han, X. Zhang, A. M. Sheveleva, Y. Cheng, F. Tuna, E. J. McInnes, L. J. McCormick McPherson, S. J. Teat, L. L. Daemen, *Nat. Chem.* **2019**, *11*, 1085–1090.
[9] A. K. Geim, K. S. Novoselov. *The rise of graphene. Nanoscience and technology: a collection of reviews from nature journals*: World Scientific; **2010**. p. 11–19.
[10] K. S. Novoselov, A. K. Geim, S. V. Morozov, D.-e. Jiang, Y. Zhang, S. V. Dubonos, I. V. Grigorieva, A. A. Firsov, *Science* **2004**, *306*, 666–669.
[11] K. M. Yam, N. Guo, Z. Jiang, S. Li, C. Zhang, *Catalysts* **2020**, *10*, 53.
[12] O. Leenaerts, B. Partoens, F. Peeters, *Phys. Rev. B* **2008**, *77*, 125416.
[13] Y. Zou, F. Li, Z. Zhu, M. Zhao, X. Xu, X. Su, *The European Physical Journal B* **2011**, *81*, 475–479.
[14] M. Zhou, Y.-H. Lu, Y.-Q. Cai, C. Zhang, Y.-P. Feng, *Nanotechnology* **2011**, *22*, 385502.
[15] H. Wang, Q. Wang, Y. Cheng, K. Li, Y. Yao, Q. Zhang, C. Dong, P. Wang, U. Schwingenschlögl, W. Yang, *Nano Lett.* **2012**, *12*, 141–144.
[16] X. Cao, X. F. Li, W. Hu, *Chemistry – An Asian Journal* **2018**, *13*, 3239–3245.
[17] J. Dai, J. Yuan, *Phys. Rev. B* **2010**, *81*, 165414.
[18] A. Akça, H. Küçük, O. Karaman, C. Karaman, N. Atar, M. L. Yola, *ECS Journal of Solid State Science and Technology* **2021**, *10*, 101008.
[19] A. Genç, H. Küçük, I. Alp, A. Akça, *Int. J. Hydrogen Energy* **2020**, *45*, 33407–33418.
[20] H. Küçük, A. Akca, *Comput. Theor. Chem.* **2022**, *1208*, 113539.
[21] H. Basharnavaz, A. Habibi-Yangjeh, S. H. Kamali, *Phys. Lett. A* **2020**, *384*, 126057.
[22] Z. Gao, L. Li, H. Huang, S. Xu, G. Yan, M. Zhao, Z. Ding, *Appl. Surf. Sci.* **2020**, *527*, 146939.
[23] H. Cui, P. Jia, X. Peng, *Appl. Surf. Sci.* **2020**, *513*, 145863.
[24] C.-S. Huang, A. Murat, V. Babar, E. Montes, U. Schwingenschlögl, *J. Phys. Chem. CC* **2018**, *122(26)*, 14665–14670.
[25] M. D. Esrafili, *Phys. Lett. A* **2019**, *383*, 1607–1614.
[26] D. Ma, J. Zhang, X. Li, C. He, Z. Lu, Z. Lu, Z. Yang, Y. Wang, *Sens. Actuators B* **2018**, *266*, 664–673.
[27] Y. Shen, X. Ge, M. Chen, *RSC Adv.* **2016**, *6*, 8469–8482.
[28] Y. Lee, S. Lee, Y. Hwang, Y.-C. Chung, *Appl. Surf. Sci.* **2014**, *289*, 445–449.
[29] B. Tian, S. Ma, Y. Zhan, X. Jiang, T. Gao, *Appl. Surf. Sci.* **2021**, *541*, 148460.
[30] H.-Y. Zhuo, X. Zhang, J.-X. Liang, Q. Yu, H. Xiao, J. Li, *Chem. Rev.* **2020**, *120*, 12315–12341.
[31] M. Luo, Z. Liang, S. G. Peera, M. Chen, C. Liu, H. Yang, J. Liu, U. P. Kumar, T. Liang, *Appl. Surf. Sci.* **2020**, *525*, 146480.
[32] T. Kaewmaraya, L. Ngamwongwan, P. Moontragoon, W. Jarernboon, D. Singh, R. Ahuja, A. Karton, T. Hussain, *J. Hazard. Mater.* **2021**, *401*, 123340.
[33] S. Marutheeswaran, S. B. Mishra, S. C. Roy, B. Nanda, *J. Phys. Chem. C* **2020**, *124*, 8786–8794.
[34] W. Zhang, K. Mao, X. C. Zeng, *ACS Sustainable Chem. Eng.* **2019**, *7*, 18711–18717.
[35] S. Impeng, A. Junkaew, P. Maitarad, N. Kungwan, D. Zhang, L. Shi, S. Namuangruk, *Appl. Surf. Sci.* **2019**, *473*, 820–827.
[36] M. Chen, X. Li, F. Yang, B. Li, T. Stracensky, S. Karakalos, S. Mukerjee, Q. Jia, D. Su, G. Wang, *ACS Catal.* **2020**, *10*, 10523–10534.
[37] Z. Lu, G. Xu, C. He, T. Wang, L. Yang, Z. Yang, D. Ma, *Carbon* **2015**, *84*, 500–508.
[38] T. Xie, P. Wang, C. Tian, G. Zhao, J. Jia, C. He, C. Zhao, H. Wu, *Molecules* **2022**, *27*, 2315.
[39] Z. Lu, M. Yang, D. Ma, P. Lv, S. Li, Z. Yang, *Appl. Surf. Sci.* **2017**, *426*, 1232–1240.

[40] M. Luo, Z. Liang, M. Chen, C. Liu, X. Qi, S. G. Peera, J. Liu, T. Liang, *New J. Chem.* **2020**, *44*, 15724–15732.
[41] M. Liu, C. Liu, S. Gouse Peera, T. Liang, *Chem. Phys.* **2022**, *559*, 111536.
[42] Y. Yang, K. Mao, S. Gao, H. Huang, G. Xia, Z. Lin, P. Jiang, C. Wang, H. Wang, Q. Chen, *Adv. Mater.* **2018**, *30*, 1801732.
[43] L. Han, M. Hou, P. Ou, H. Cheng, Z. Ren, Z. Liang, J. A. Boscoboinik, A. Hunt, I. Waluyo, S. Zhang, *ACS Catal.* **2020**, *11*, 509–516.
[44] P. Giannozzi, O. Andreussi, T. Brumme, O. Bunau, M. B. Nardelli, M. Calandra, R. Car, C. Cavazzoni, D. Ceresoli, M. Cococcioni, *J. Phys. Condens. Matter* **2017**, *29*, 465901.
[45] P. Giannozzi, S. Baroni, N. Bonini, M. Calandra, R. Car, C. Cavazzoni, D. Ceresoli, G. L. Chiarotti, M. Cococcioni, I. Dabo, *J. Phys. Condens. Matter* **2009**, *21*, 395502.
[46] X. Liao, R. Lu, L. Xia, Q. Liu, H. Wang, K. Zhao, Z. Wang, Y. Zhao, *Energy Environ.* **2022**, *5*, 157–185.
[47] P. E. Blöchl, *Phys. Rev. B* **1994**, *50*, 17953.
[48] G. Kresse, D. Joubert, *Phys. Rev. B* **1999**, *59*, 1758.
[49] J. P. Perdew, K. Burke, M. Ernzerhof, *Phys. Rev. Lett.* **1996**, *77*, 3865.
[50] H. J. Monkhorst, J. D. Pack, *Phys. Rev. B* **1976**, *13*, 5188.
[51] G. Henkelman, A. Arnaldsson, H. Jónsson, *Comput. Mater. Sci.* **2006**, *36*, 354–360.
[52] E. Sanville, S. D. Kenny, R. Smith, G. Henkelman, *J. Comput. Chem.* **2007**, *28*, 899–908.
[53] W. Tang, E. Sanville, G. Henkelman, *J. Phys. Condens. Matter* **2009**, *21*, 084204.
[54] R. F. Bader, T. Nguyen-Dang. Quantum theory of atoms in molecules-Dalton revisited. Advances in Quantum Chemistry. 14: Elsevier; **1981**. p. 63–124.
[55] C. F. Matta, R. J. Boyd, *The quantum theory of atoms in molecules: from solid state to DNA and drug design*, **2007**.
[56] M. Ziółkowski, S. J. Grabowski, J. Leszczynski, *J. Phys. Chem. A* **2006**, *110*, 6514–6521.
[57] S. M. Soliman, A. Barakat, *Molecules* **2016**, *21*, 1669.
[58] S. Borocci, M. Giordani, F. Grandinetti, *J. Phys. Chem. A* **2015**, *119*, 6528–6541.
[59] C. Gatti, *Zeitschrift für Kristallographie-Crystalline Materials* **2005**, *220*, 399–457.
[60] J. Klein, P. Fleurat-Lessard, J. Pilmé, *J. Comput. Chem.* **2021**, *42*, 840–854.
[61] D. Kozlowski, J. Pilme, *J. Comput. Chem.* **2011**, *32*, 3207–3217.
[62] V. L. Deringer, A. L. Tchougréeff, R. Dronskowski, *J. Phys. Chem. A* **2011**, *115*, 5461–5466.
[63] R. Dronskowski, P. E. Bloechl, *J. Phys. Chem.* **1993**, *97*, 8617–8624.
[64] R. Y. Rohling, I. C. Tranca, E. J. Hensen, E. A. Pidko, *J. Phys. Chem. C* **2018**, *122*, 14733–14743.
[65] R. Y. Rohling, I. C. Tranca, E. J. Hensen, E. A. Pidko, *J. Phys. Chem. C* **2019**, *123*, 2843–2854.
[66] R. Van Santen, I. Tranca, *Phys. Chem. Chem. Phys.* **2016**, *18*, 20868–20894.
[67] R. A. van Santen, I. Tranca, E. J. Hensen, *Catal. Today* **2015**, *244*, 63–84.
[68] P. C. Müller, C. Ertural, J. Hempelmann, R. Dronskowski, *J. Phys. Chem. CC* **2021**, *125*, 7959–7970.
[69] K. B. Wiberg, *Tetrahedron* **1968**, *24*, 1083–1096.
[70] I. Mayer, *Chem. Phys. Lett.* **1983**, *97*, 270–274.
[71] S. Maintz, V. L. Deringer, A. L. Tchougréeff, R. Dronskowski. LOBSTER: A tool to extract chemical bonding from plane-wave based DFT. Wiley Online Library; 2016.
[72] S. J. Clark, M. D. Segall, C. J. Pickard, P. J. Hasnip, M. I. Probert, K. Refson, M. C. Payne, *Zeitschrift für kristallographie-crystalline materials* **2005**, *220*, 567–570.
[73] V. Bermudez, *J. Phys. Chem. C* **2020**, *124*, 15275–15284.
[74] H. Ma, L. Ma, L.-C. Ma, *Int. J. Mod. Phys. B* **2019**, *33*, 1950166.
[75] A. L. Görne, R. Dronskowski, *Carbon* **2019**, *148*, 151–158.
[76] H. Iriawan, S. Z. Andersen, X. Zhang, B. M. Comer, J. Barrio, P. Chen, A. J. Medford, I. E. Stephens, I. Chorkendorff, Y. Shao-Horn, *Nature Reviews Methods Primers* **2021**, *1*, 1–26.
[77] P. Liu, C. Fu, Y. Li, H. Wei, *Phys. Chem. Chem. Phys.* **2020**, *22*, 9322–9329.
[78] X.-F. Li, Q.-K. Li, J. Cheng, L. Liu, Q. Yan, Y. Wu, X.-H. Zhang, Z.-Y. Wang, Q. Qiu, Y. Luo, *J. Am. Chem. Soc.* **2016**, *138*, 8706–8709.
[79] D. V. Yandulov, R. R. Schrock, *Science* **2003**, *301*, 76–78.
[80] E. Dražević, E. Skúlason, *iScience* **2020**, *23*, 101803.
[81] P. S. V. Kumar, V. Raghavendra, V. Subramanian, *J. Chem. Sci.* **2016**, *128*, 1527–1536.
[82] M. Yu, D. R. Trinkle, *J. Chem. Phys.* **2011**, *134*, 064111.

Submitted: November 23, 2022
Accepted: March 17, 2023